Origin of underwater oil-repellence in polyelectrolyte brush surfaces

Dan Daniel,* Shermin Simin Goh, Truong Ngoc Bao Tran, Xue Qi Koh, and Nikodem Tomczak†
*Institute of Materials Research and Engineering, A*STAR (Agency for Science, Technology and Research), 2 Fusionopolis Way, Innovis, Singapore 138634*

When submerged under water, polyelectrolyte brush surfaces become highly oil-repellent. This is due to the ability of the charged moieties on the polymer backbone to retain strong hydration shells. Despite their technological relevance, there is no rational design principle for optimizing the oil-repellent performance of hydrophilic polyelectrolyte brushes. Using droplet probe Atomic Force Microscopy (AFM), we measured the interaction forces between an oil droplet and different polyelectrolyte brushes. We show that surfaces are most repellent when there are repulsive electric double-layer forces that can stabilize a continuous water film beneath the oil droplet. Once a stable hydration layer forms, the oil-repellent performance is not affected by the polymer brush characteristics, such as its thickness and swelling ratio.

There is a huge interest in developing superoleophobic surfaces for various applications, such as in anti-fouling coatings and oil-water separation membranes [1, 2]. Polyelectrolyte brush surfaces have received much attention because of their ability to repel oil under water even in the absence of micro-/nano-structures [3–5]. Polyelectrolyte brushes swell under water and retain hydration shells around their charged moieties, resulting in extreme oil-repellence. It is thought that the presence of such strong hydration shells also accounts for the ability of polyelectrolyte brushes to resist fouling [6] and to greatly reduce sliding friction (e.g. between cartilage surfaces in skeletal joints) [7, 8]. Despite the recent progress, many outstanding questions on the brushes' oil-repellent properties remain unanswered [3, 9]. For example, it is not known how the details of the polymer brush layer, such as its thickness, grafting density, and chemical structure of the charged groups, translate to its oil-repellent performance. The relationship between polymer brush hydrophilicity in air and its oleophobicity under water is also not clear.

In this article, we use droplet probe Atomic Force Microscopy (AFM) to directly measure the interaction forces between an oil microdroplet and polyelectrolyte brushes of varied chemical structure [10–12]. We show that for brushes with anionic and zwitterionic moieties, there is repulsion between the droplet and the brush layer, whose origin we attribute to electric double-layer forces. There is maximal oil-repellence when the repulsive forces are sufficiently strong to stabilize a water film (hundreds of nanometres thick) beneath the droplet. Critically, this repellence does not depend on the specific characteristics of the brush layer (e.g. exact chemical moiety or thickness). This is in sharp contrast to the friction-reducing properties of polymer brushes, which are highly dependent on the brush architecture [8, 13, 14].

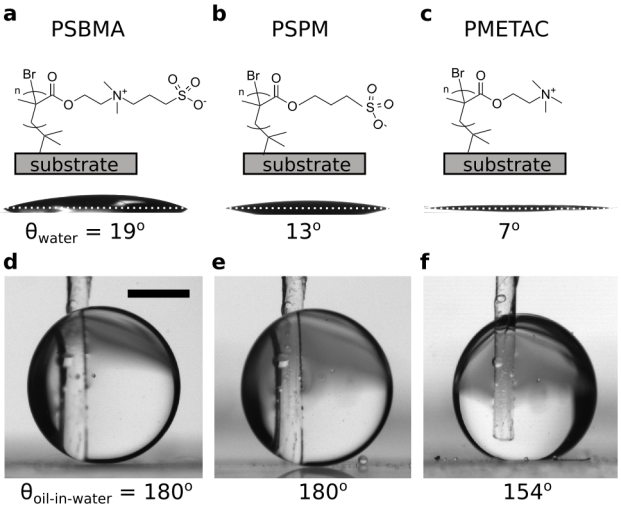

FIG. 1. (a)–(c) Water droplet makes a contact angle $\theta_{\text{water}} = 19\pm3^\circ$, $13\pm3^\circ$, and $7\pm2^\circ$ on PSBMA, PSPM, and PMETAC brush surfaces in air, respectively. (d), (e) When submerged under water, a silicone oil droplet makes a contact angle of $\theta_{\text{oil-in-water}} = 180^\circ$ on PSBMA and PSPM surfaces, (f) and $\theta_{\text{oil-in-water}} = 154\pm4^\circ$ on the PMETAC surface. Uncertainties in θ measurements are the standard deviations calculated for three repeats. Scale bar is 1 mm.

RESULTS AND DISCUSSIONS

We compare the properties of three polyelectrolyte brush surfaces with zwitterionic, anionic, and cationic moieties (Fig. 1a–c), specifically poly(sulfobetaine methacrylate) (PSBMA), poly[(2-methacryloyloxyethyl) trimethylammonium chloride] (PMETAC), and poly(3-sulfopropyl methacrylate) (PSPM) brushes, respectively. The brushes were grown on glass slides using surface-initiated Atom Transfer Radical Polymerization (ATRP) techniques, and their thicknesses were controlled from tens to hundreds of nanometres by varying the polymerization time. The resulting dry and wet film thicknesses in air and water $h_{\text{dry, wet}}$ were measured using AFM, as

* daniel@imre.a-star.edu.sg
† tomczakn@imre.a-star.edu.sg

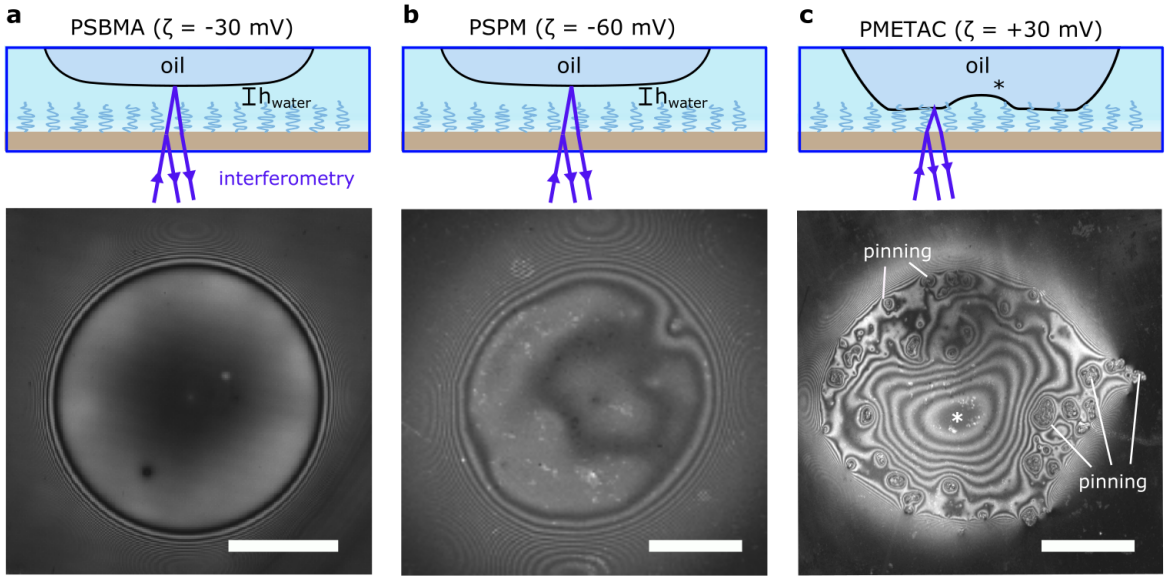

FIG. 2. (a), (b) For PSBMA and PSPM surfaces, there is a continuous water film separating the base of the oil droplet and the underlying polymer brush, as visualized using Reflection Interference Contrast Microscopy. (c) For PMETAC surface, this hydration film is only partial. There are locations where the oil droplet is in contact with the polymer brushes resulting in visible pinning points. Scale bars are 200 μm, 100 μm, and 250 μm, for (a)–(c) respectively. Interferograms were taken 20 minutes after the droplet was placed on the brush surfaces to allow sufficient time for water beneath the droplet to drain out.

summarized in Table I. See Materials and Methods for details. Because of the very different growth rates of different brushes, it is difficult to have the same thicknesses for the three brushes. In any case, as we will show in this paper, the oil-repellent properties are not sensitive to the exact brush layer thickness.

TABLE I. Brush properties for Figures 1–4. Uncertainties in $h_{\mathrm{dry,\ wet}}$ are due to roughness as measured using AFM.

	h_{dry} (nm)	h_{wet} (nm)	$h_{\mathrm{wet}}/h_{\mathrm{dry}}$	θ_{water}
PSBMA	7 ± 2	14 ± 2	2 ± 0.8	19 ± 3°
PSPM	96 ± 3	130 ± 10	1.4 ± 0.2	13 ± 2°
PMETAC	176 ± 3	780 ± 30	4.4 ± 0.2	7 ± 2°

All the polyelectrolyte brushes in this study are hydrophilic, with low contact angles for water droplet in air $\theta_{\mathrm{water}} < 20°$. The brushes swell under water, though with different swelling ratios $h_{\mathrm{wet}}/h_{\mathrm{dry}} = 1.4$–$4.4$, likely due to different grafting densities [15]. When submerged under water, both PSMBA and PSPM surfaces are equally oil-repellent; on both surfaces, a millimetric-sized silicone oil droplet has a contact angle $\theta_{\mathrm{oil\text{-}in\text{-}water}} = 180°$. In contrast, PMETAC is less oil-repellent with $\theta_{\mathrm{oil\text{-}in\text{-}water}} = 154 \pm 4\ °$, despite having the highest swelling ratio (and therefore water content) and lowest $\theta_{\mathrm{water}} = 7 \pm 2°$ (Fig. 1 and Table I). The most hydrophilic brush surface in air is therefore not necessarily the most oleophobic one under water.

To achieve the maximal oil-repellence, the brush surface must be able to stabilize a continuous water film beneath the oil droplet, which we can confirm using Reflection Interference Contrast Microscopy (RICM) [16, 17]. We shone monochromatic light of wavelength λ=561 nm from below the brush and captured the reflection off the droplet base (Fig. 2). The presence of the water film results in thin-film interference and, in particular, dark and bright fringes as light reflected off the various interfaces interfere destructively and constructively. Details of the method can be found in our previous publications [9].

Previously, we showed that PSBMA surfaces with zwitterionic moieties can stabilize such a hydration film [9]. This is because both oil droplet and the brush surface acquire negative surface charges in water, with reported zeta potentials of -40 mV and -30 mV, respectively [11, 18, 19]. The negative charges generate repulsive electric double-layer forces and result in a water film layer as thick as $h_{\mathrm{water}} = 200$ nm [9, 20].

Here, we found the same stable water film for PSPM surfaces with anionic moieties, which are known to be negatively charged with reported zeta potential of -60 mV [21]. There is no contact (and hence no contact line pinning) between droplet and the substrate for both PSBMA and PSPM surfaces. As a result, the droplet's base is smooth and circular in shape (Fig. 2a, b).

In contrast, PMETAC brushes with cationic moieties become positively charged under water, with a reported zeta potential of +30 mV [22]. The electric double-layer forces are now attractive and as a result, there is only a partial hydration film, as evident from the interference

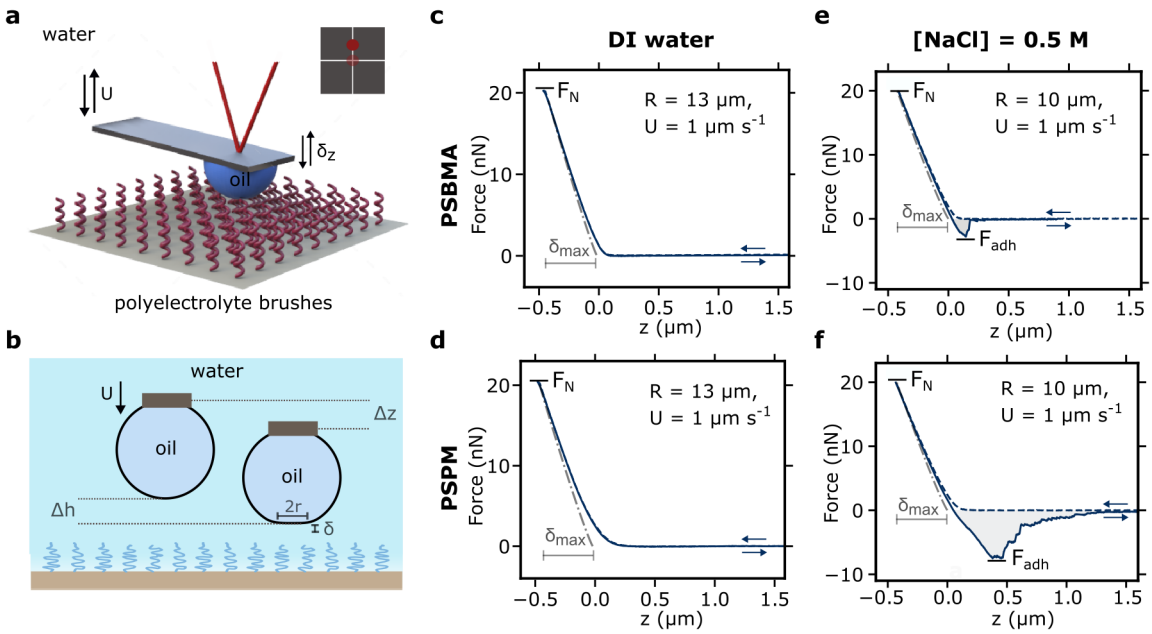

FIG. 3. (a) Schematic of droplet probe AFM setup used to quantify droplet-surface interactions. (b) Separation distance between droplet's base and the brushes h depends on the piezo-positioning of the AFM z (after correcting for cantilever deflection) and also the deformation of the droplet's base δ, more precisely $\Delta h = \Delta z$ - δ. (c, d) Force spectroscopy results for oil droplets of radius $R = 13$ μm in DI water for PSBMA and PSPM surfaces. (e, f) Force spectroscopy results for oil droplets of radius $R = 10$ μm in 0.5M NaCl salt solution for PSBMA and PSPM surfaces.

fringes in Figure 2c. The oil droplet is in contact with the surface at certain regions, creating pinning points. As a result, the outline of droplet's base is jagged and irregularly shaped. Note that because of slow drainage dynamics [23], there is still a micron-thick puddle of water trapped beneath the droplet after twenty minutes (marked by an asterisk in Figure 2c).

The intermolecular forces between the oil droplet and the polyelectrolyte brushes can be probed directly using droplet probe AFM. We attached a silicone oil droplet (tens of micron in size) onto a tipless cantilever probe with a flexular spring constant of $k_z = 0.2$–2 N m^{-1} (Fig. 3a). The force acting on the droplet F was obtained from the cantilever deflection δ_z, since $F = k_z\delta_z$ [12, 24].

For conventional AFM with a sharp solid tip, the separation distance h between the solid tip and the surface is equivalent to the piezo-positioning z (after corecting for δ_z) of the AFM [24]. For droplet probe AFM, however, we have to additionally account for droplet deformation in the z-direction δ, i.e. $\Delta h = \Delta z - \delta$ (Fig. 3b). Note that the deformation of the brush layer is minimal, since the Young's moduli of the polyelectrolyte brushes E (between 100 and 300 kPa [25]) are much higher than the Laplace pressure $2\gamma/R \approx 6$ kPa exerted by the droplet.

Figures 3c, d show the force experienced by an oil droplet of radius $R = 13$ μm as a function of z (which is not the separation distance), as it approaches (dashed line) and retracts (full line) from PSBMA and PSPM surfaces at a speed of $U = 1$ μm s^{-1} in deionized (DI) water.

We can relate the loading force F acting on the droplet to its deformation δ by noting that $F = (2\gamma/R)\pi r^2$, where R is the droplet's radius, r is the droplet's base radius, and γ is the interfacial tension. Using scaling arguments, we expect $r \sim \sqrt{R\delta}$, and hence $F \sim \gamma\delta$: the droplet deforms like a Hookean spring system with γ playing the role of the spring constant. The droplet deformation can be more rigorously modelled by solving the axisymmetric Young-Laplace equation numerically and we found that

$$F = 1.9\,\gamma R^{-0.1}\delta^{1.1}, \tag{1}$$

which we have plotted as gray dashed-dot lines (with no fitting parameters) up to the maximum loading force $F_N = 20$ nN in Figures 3c–f. Our choice of z=0 corresponds to the point when the droplet starts to deform; the maximum deformation experienced by the droplet $\delta_{max} < 0.5$ μm is a small fraction of the droplet's diameter, which justifies our initial Hookean assumption. Note that our numerical result in Equation 1 differs slightly from our simplified Hookean analysis. In particular, F is only approximately linear to δ and depends weakly on the droplet size R. Details on how we implement the numerical calculations can be found in Supplementary Figures S1 and S2, and our github repository [26].

At a slow speed of $U = 1$ μm s^{-1}, viscous effects are unimportant—we know this because viscous forces are non-conservative and should result in a hysteresis loop in the approach and retract curves. Instead, we find that the two curves overlap with each other.

The repulsive force $F > 0$ experienced by the droplet can be explained by a combination of droplet deformation (with the dashed-dot lines representing the numerical solution in equation 1) and electric double-layer forces, which can have a range of interaction of more than 100 nm in DI water [9, 20]. PSPM brushes, which have larger zeta potential than PSBMA (-60 mV and -30 mV, respectively), exhibit more repulsive double-layer forces, as indicated by the larger departure from equation 1. It is difficult to model double-layer forces in DI water, because the ion concentration between the two interfaces is sensitive to surface charge and can differ greatly from bulk concentration. In any case, the repulsive double-layer force prevents contact of the brushes with the droplet. As a result, there is no adhesion of the droplet to the surface and minimal energy dissipation.

Dissolved salt ions can however screen the electric double-layer forces and the droplet can now come into contact with the brush layer. As a result, both PSBMA and PSPM brushes are less oil-repellent when submerged in 0.5M NaCl solution (Figs. 3e, f). There is now a maximum adhesion force that must be overcome to remove the droplet $F_{\rm adh} = 2.4$ and 5.8 nN—as well as a total work done to overcome contact-line pinning $W = 9.5 \times 10^{-16}$J and 2.5×10^{-15}J (shaded areas in Figures 3e, f)—for PSBMA and PSPM brushes, respectively. Note that since dissipative forces due to contact-line pinning are non-conservative, W is not the work of adhesion, which is typically defined as the reversible thermodynamic work required to separate the interface between two phases.

Unlike PSBMA and PSPM, PMETAC surface is positively charged and therefore unable to sustain a continuous water layer even in DI water. As a result, there is a sudden snap-in force $F_{\rm snap} = 50$ nN at $z = 0$ when the oil droplet of radius $R = 10$ μm first contacts the brushes. There is now contact line pinning and consequently, PMETAC has a much larger $F_{\rm adh} = 145$ nN and $W = 5.6 \times 10^{-13}$J (Fig. 4a). Note that although PMETAC surface does not perform as well as PSBMA and PSPM, it is still highly oil-repellent. The experimentally obtained value of W is still a small fraction (about 1 %) of the total surface energy of the droplet $4\pi R^2\gamma = 5 \times 10^{-11}$J and is comparable to energy required to remove a water droplet of similar size on superhydrophobic surfaces [12].

A closer inspection of the approach curve also reveals a small repulsive force of about 1 nN just before the snap-in force $F_{\rm snap}$ (Fig. 4b). Since viscous effects are minimal at $U = 1$ μm s^{-1}, the presence of a repulsive force could be due to the fact that to contact the brush layer, the droplet must displace the hydration shells that surround the positively-charged quaternary ammonium cation [27, 28].

So far, we have discussed the force spectroscopy results in the limit of low velocity $U = 1$ μm s^{-1}. As we increase U to 20 μm s^{-1}, viscous effects become important. As the droplet approaches the surface, water beneath the oil

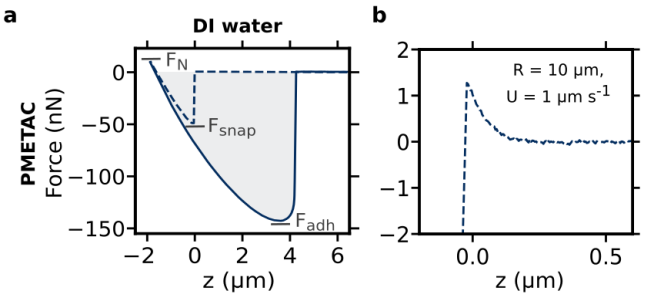

FIG. 4. (a) Force spectroscopy curve for an oil droplet of radius $R = 10$ μm in DI water for PMETAC surfaces. (b) Just before the droplet snaps onto the surface, there is a small repulsive force.

droplet has to drain out, resulting in a repulsive force; when the droplet retracts, water flows back in, resulting in suction and an effective adhesion force $F_{\rm adh}$ [29]. As a result, there is now a hysteresis loop in the force spectroscopy curves for 26-μm-sized droplet on PSBMA and PSPM surfaces (Fig. 5a, b). The measured $F_{\rm adh} \approx 1$ nN (due to hydrodynamic viscous effects) on PSBMA and PSPM surfaces are still much smaller than $F_{\rm adh} = 120$ nN (due to the formation and subsequent breakup of capillary bridge) for a similarly-sized droplet on PMETAC surface (Fig. 5c).

In the absence of contact-line pinning on PSBMA and PSPM surfaces (blue filled and empty markes in Fig. 5d and e, respectively), $F_{\rm adh}$ increases from less than 1 nN to more than 100 nN as we vary the speed U=1–200 μm s^{-1} for droplets of size $R = 20$, 60 μm (circle and square markers, respectively). In contrast, for PMETAC surfaces (Fig. 5f) and interestingly also for PSBMA surface in salt solution (red triangles in Figure 5d), contact-line pinning dominates and $F_{\rm adh}$ no longer depends on U.

Previously, we showed that $F_{\rm adh}$ due to hydrodynamic viscous effects should scale as

$$F_{\rm adh}/2R\gamma \sim Ca^{\nu}, \tag{2}$$

where $Ca = \eta U/\gamma$ is the capillary number, η is water's viscosity, and ν is some unknown exponent [9]. Previously, we also found that $\nu = 0.6$ best fits the experimental results for millimetric-sized droplets of size $R =$ 1–3 mm [9]. Here, we found that $\nu = 0.8$ best explains the $F_{\rm adh}$ results for smaller droplets between $R =$ 15–60 μm (full line in Figure 5g).

To obtain the exact value of ν would require us to solve the Young-Laplace and Navier-Stokes equation fully, either analytically and numerically, which is outside the scope of this work. Nonetheless, equation 2 captures the main physical insights: in the presence of a hydration film, $F_{\rm adh}$ increases linearly with droplet's size R and non-linearly with speed U, but does not depend on the details of the brush film, such as its thickness or exact chemical moiety. Experimentally, we found that once $F_{\rm adh}$ is non-dimensionalized as $F_{\rm adh}/2R\gamma$, the experimen-

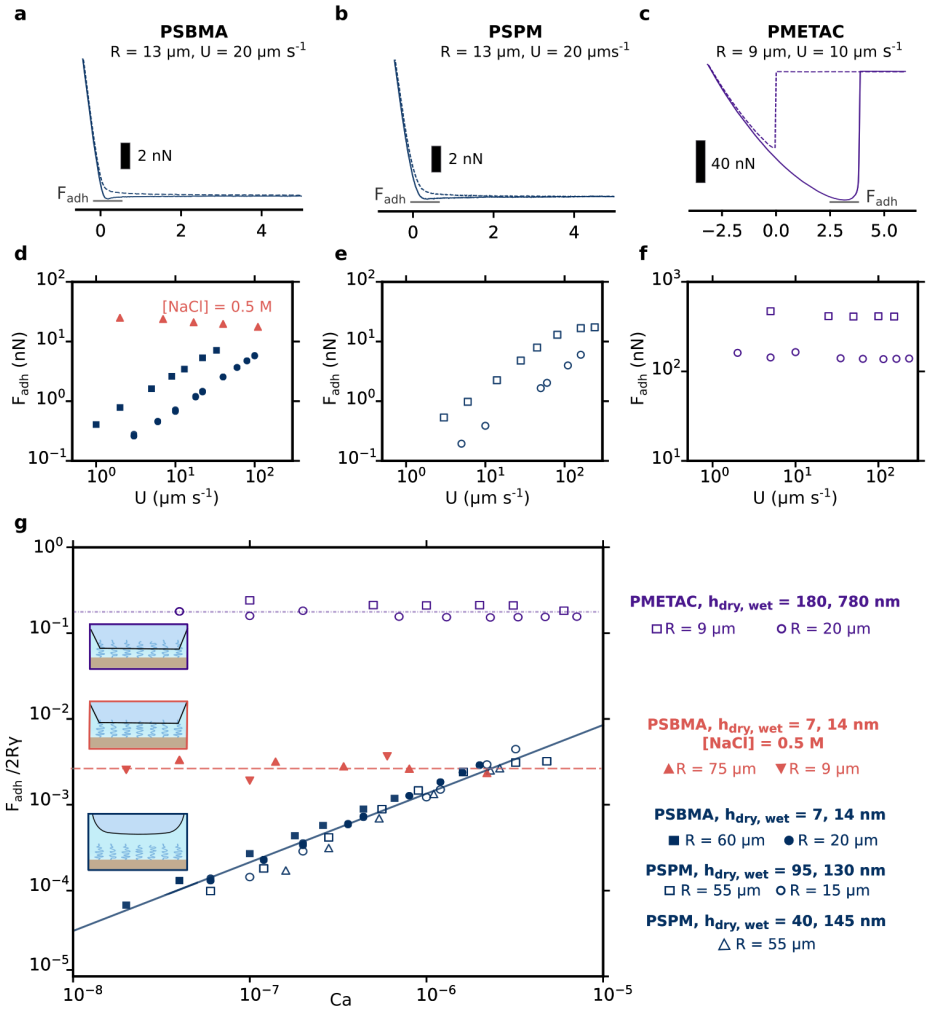

FIG. 5. (a–c) Force spectroscopy results for PSBMA, PSPM, and PMETAC surfaces. (d–f) F_{adh} measurements for droplets of different sizes R = 9–60μm, different brushes of varying thicknesses. (g) All the F_{adh} results can be presented in the non-dimensionalized form $F_{\mathrm{adh}}/2R\gamma$ vs. Ca, where Ca is the capillary number.

tal results for PSBMA and PSPM brushes with very different thicknesses ($h_{\mathrm{dry}} = 7 - 95$ nm, $h_{\mathrm{wet}} = 14 - 145$ nm) and swelling ratios (between 2 and 4) overlap with one another (Figure 5g).

The differences in the oil-repellent performance of polyelectrolyte surfaces without a stable hydration film (dashed lines) when compared to those with a stable film (full line) are summarized by the non-dimensional plot in Figure 5g. In the absence of a stable hydration film, F_{adh} no longer depends on U and can be a hundred times or even a thousand times higher (for example, PMETAC surface in DI water) for similarly-sized droplets.

CONCLUSIONS

In this work, we have shed light on the design principle for optimal underwater oil-repellent performance of polyelectrolyte brush surfaces: brushes should have a negative zeta potential which can stabilize a water film beneath the oil droplet. Once the hydration layer is present, the oil-repellent performance is insensitive to the details of the polyelectrolyte brushes. We also found that oil-repellent performance is reduced in the presence of salt, which tend to screen surface charges. How best to improve the oil-repellent performance when the presence of salts is unavoidable, such as in marine environments, remains an open question, which may require strategies beyond simple hydration and electrical double layers.

ACKNOWLEDGEMENTS

The authors are grateful to the Agency for Science, Technology and Research (A*STAR) for providing financial support under the SERC Career Development Award (grant number A1820g0089) and Pharos Advanced Surfaces Programme (grant number 1523700101).

MATERIALS AND METHODS

Materials and chemicals. (3-trimethoxysilyl)-propyl 2-bromo-2-methylpropionate (Br-initiator, 95 %) was purchased from Gelest Inc. [2-(methacryloyloxy)ethyl]dimethyl-(3-sulfopropyl) ammonium hydroxide (SBMA, $\geq$ 96 %), 3-sulfopropyl methacrylate potassium (SPM, $\geq$ 98 %), 2-(methacryloyloxy)ethyl trimethylammonium chloride (METAC, 75 wt. % in water), copper(I) bromide (CuBr, $\geq$ 98%), and 2,2-bipyridine (bipy, $\geq$ 99 %) were purchased from Sigma-Aldrich. Methanol was purchased from J.T. Baker. Silicone oil (polyphenylmethylsiloxane, viscosity $\sim$ 100 mPa.s, density 1.06g/ml) was purchased from Sigma-Aldrich. The water-oil interfacial tensions is 35 mN/m as measured using the pendant drop method. All chemicals were used as received. Deionized water with a resistivity of 18.2 MΩ.cm was obtained from a Milli-Q water purification system (Millipore, Bedford, MA, USA).

Surface preparation. The polymer brush surfaces were prepared using surface initiated Atom Transfer Radical Polymerization (ATRP) using a protocol adapted from Azzaroni *et al.* (2006) for PSBMA [30] and Oh *et al.* (2019) for PSPM and PMETAC [31].

Purification of CuBr. CuBr was stirred in glacial acetic acid for 8 hours, then filtered, washed with ethanol and diethyl ether. The off-white solid obtained was then dried in the oven overnight at 70°C under vacuum [32].

Initiator monolayer deposition. The surfaces (glass or silicon wafer) were sonicated in deionized (DI) water, acetone and isopropanol sequentially before drying under a nitrogen stream. The dried surfaces were then subjected to oxygen plasma surface cleaning at 150 W for 120 s. Br-initiator was vapour deposited onto the cleaned surfaces. In a typical procedure, the cleaned surfaces were heated in a vacuum oven at 75°C with the Br-initiator (100 μL) overnight. The dried silanized surfaces were then heated in an oven at 110°C for 20 minutes.

PSBMA brush growth. SBMA salt (15 g, 54 mmol) and bipy (210 mg, 1.3 mmol) were dissolved in a mixture of methanol (40 mL) and deionized water (10 mL). The mixture was stirred, degassed and flushed with argon for 20 minutes. Purified CuBr (77 mg, 0.5 mmol) was then added. Stirring of this polymerisation precursor solution continued under argon atmosphere for a further 2 minutes. Each glass or silicon substrate coated with ATRP initiator was placed in an individual vial and purged with argon. The polymerisation precursor solution (4.5 mL) was syringed into the vials, ensuring that the substrate was completely covered by the solution. The polymerisation was allowed to proceed for the required time under argon atmosphere. Growth rate is about 20 nm per hour. After polymerisation, the substrates were washed with deionized water at 60°C and dried with a stream of nitrogen.

PSPM brush growth. SPM salt (1.5 g, 6.1 mmol) and bipy (63 mg, 0.40 mmol) were dissolved in a mixture of in methanol (6 mL) and deionized water (3 mL). The mixture was stirred, degassed and flushed with argon for 20 minutes. Purified CuBr (29 mg, 0.20 mmol) was then added. Stirring of this polymerisation precursor solution under argon atmosphere continued for a further 2 minutes. Each glass or silicon substrate coated with ATRP initiator was placed in an individual vial and purged with argon. The polymerisation precursor solution (4.5 mL) was syringed into the vials, ensuring that the substrate was completely covered by the solution. The polymerisation was allowed to proceed for the required time under argon atmosphere. Growth rate is about 40 nm per hour. After polymerisation, the substrates were washed with deionized water at 60°C and dried with a stream of nitrogen.

PMETAC brush growth. 2-(methacryloyloxy)ethyl trimethylammonium chloride (METAC) (3.5 g, 17 mmol) was passed through an alumina column and then dissolved in a mixture of water (1 mL) and isopropanol (4 mL). The mixture was stirred, degassed, and flushed with argon for 20 minutes. Purified CuBr (36 mg, 0.25 mmol) and bipy (95 mg, 0.61 mmol) were added. This polymerisation precursor solution was stirred and flushed under argon for another 10 minutes. Each glass or silicon substrate coated with ATRP initiator was placed in an individual vial and purged with argon. The polymerisation precursor solution (4.5 mL) was syringed into the vials, ensuring that the substrate was completely covered by the solution. The polymerisation was allowed to proceed for the required time under argon atmosphere. Growth rate is about 170 nm per hour. After polymerisation, the substrates were washed with deionized water at 60°C and dried with a stream of nitrogen.

Determining brush thickness. The dry and wet thicknesses of the polymer brush layer on a silicon wafer can be determined using either ellipsometry or Atomic Force Microscopy (AFM). Both techniques give similar results. For brush layer on glass, the thickness can only determined using AFM, as the refractive index contrast between the brush layer and glass is too small for accurate ellipsometry measurement. Details can be found in Daniel *et al.* (2019) [9].

Droplet probe AFM. To create small oil droplets, we force 50 μl of oil through a small capillary tube with inner and outer diameters of 360 μm and 290 μm into a petri-dish of water. This generates multiple droplets with a broad range of sizes $2R$ = 20—200 μm. We can then pick up a droplet of the desired size to perform force spectroscopy measurements on the surface of interest.

Details on how we calibrated the cantilevers, performed the force spectroscopy measurements, and converted the raw voltage signals on the four-quadrant sensor into force values can be found in our previous publication [12].

[1] J. Yong, F. Chen, Q. Yang, J. Huo, and X. Hou, "Superoleophobic surfaces," Chem. Soc. Rev. **46**, 4168–4217 (2017).

[2] K.-T. Huang, S.-B. Yeh, and C.-J. Huang, "Surface modification for superhydrophilicity and underwater superoleophobicity: applications in antifog, underwater self-cleaning, and oil–water separation," ACS Appl. Mater. Interfaces **7**, 21021–21029 (2015).

[3] M. Kobayashi, Y. Terayama, H. Yamaguchi, M. Terada, D. Murakami, K. Ishihara, and A. Takahara, "Wettability and antifouling behavior on the surfaces of superhydrophilic polymer brushes," Langmuir **28**, 7212–7222 (2012).

[4] M. Liu, S. Wang, Z. Wei, Y. Song, and L. Jiang, "Bioinspired design of a superoleophobic and low adhesive water/solid interface," Adv. Mater. **21**, 665–669 (2009).

[5] M. Liu, S. Wang, and L. Jiang, "Nature-inspired superwettability systems," Nat. Rev. Mater. **2**, 17036 (2017).

[6] Yuji Higaki, Motoyasu Kobayashi, Daiki Murakami, and Atsushi Takahara, "Anti-fouling behavior of polymer brush immobilized surfaces," Polymer Journal **48**, 325–331 (2016).

[7] S. Jahn, J. Seror, and J. Klein, "Lubrication of articular cartilage," Annu. Rev. Biomed. Eng. **18**, 235–258 (2016).

[8] E. B. Zhulina and M. Rubinstein, "Lubrication by polyelectrolyte brushes," Macromolecules **47**, 5825–5838 (2014).

[9] D. Daniel, A. Y. T. Chia, L. C. H. Moh, R. Liu, X. Q. Koh, X. Zhang, and N. Tomczak, "Hydration lubrication of polyzwitterionic brushes leads to nearly friction- and adhesion-free droplet motion," Comm. Phys. (2019).

[10] L. Xie, C. Shi, X. Cui, and H. Zeng, "Surface forces and interaction mechanisms of emulsion drops and gas bubbles in complex fluids," Langmuir **33**, 3911–3925 (2017).

[11] C. Shi, B. Yan, L. Xie, L. Zhang, J. Wang, A. Takahara, and H. Zeng, "Long-range hydrophilic attraction between water and polyelectrolyte surfaces in oil," Angew. Chem. Int. Ed. **55**, 15017–15021 (2016).

[12] D. Daniel, C. L. Lay, A. Sng, C. J. J. Lee, D. C. J. Neo, X. Y. Ling, and N. Tomczak, "Mapping micrometer-scale wetting properties of superhydrophobic surfaces," Proc. Natl. Acad. Sci. U.S.A. (2019).

[13] X. Banquy, J. Burdyska, D. W. Lee, K. Matyjaszewski, and J. Israelachvili, "Bioinspired bottle-brush polymer exhibits low friction and amontons-like behavior," J. Am. Chem. Soc. **136**, 6199–6202 (2014).

[14] E. M Benetti, M. Divandari, S. N. Ramakrishna, G. Morgese, W. Yan, and L. Trachsel, "Loops and cycles at surfaces: The unique properties of topological polymer brushes," Chem. Eur. J. **23**, 12433–12442 (2017).

[15] S. Yamamoto, M. Ejaz, Y. Tsujii, and T. Fukuda, "Surface interaction forces of well-defined, high-density polymer brushes studied by atomic force microscopy. 2. effect of graft density," Macromolecules **33**, 5608–5612 (2000).

[16] L. Limozin and K. Sengupta, "Quantitative reflection interference contrast microscopy (RICM) in soft matter and cell adhesion," ChemPhysChem **10**, 2752–2768 (2009).

[17] D. Daniel, J. V. I. Timonen, R. Li, S. J. Velling, and J. Aizenberg, "Oleoplaning droplets on lubricated surfaces," Nat. Phys. **13**, 1020 (2017).

[18] K. Roger and B. Cabane, "Why are hydrophobic/water interfaces negatively charged?" Angew. Chem. Int. Ed. **51**, 5625–5628 (2012).

[19] J. K Beattie, "The intrinsic charge at the hydrophobe/water interface," (2007).

[20] J. N. Israelachvili, *Intermolecular and surface forces* (Academic press, 2011) Chap. 14.

[21] G. Romero, I. Estrela-Lopis, P. Castro-Hartmann, E. Rojas, I. Llarena, D. Sanz, E. Donath, and S. E. Moya, "Stepwise surface tailoring of carbon nanotubes with polyelectrolyte brushes and lipid layers to control their intracellular distribution and in vitro toxicity," Soft Matter **7**, 6883–6890 (2011).

[22] J. Irigoyen, V. B. Arekalyan, Z. Navoyan, J. Iturri, S. E. Moya, and E. Donath, "Spherical polyelectrolyte brushes' constant zeta potential with varying ionic strength: an electrophoretic study using a hairy layer approach," Soft Matter **9**, 11609–11617 (2013).

[23] R. G. Horn, M. Asadullah, and J. N. Connor, "Thin film drainage: hydrodynamic and disjoining pressures determined from experimental measurements of the shape of a fluid drop approaching a solid wall," Langmuir **22**, 2610–2619 (2006).

[24] H.-J. Butt, B. Cappella, and M. Kappl, "Force measurements with the atomic force microscope: Technique, interpretation and applications," Surf. Sci. Rep. **59**, 1–152 (2005).

[25] E. Kutnyanszky and G. J. Vancso, "Nanomechanical properties of polymer brushes by colloidal afm probes," Eur. Polym. J. **48**, 8–15 (2012).

[26] D. Daniel, "Simulating droplet compression," `https://github.com/ddaniel331/simulating_compression` (2020), accessed: 2020-07-01.

[27] D. Laage, T. Elsaesser, and J. T. Hynes, "Water dynamics in the hydration shells of biomolecules," Chem. Rev. **117**, 10694–10725 (2017).

[28] O. Azzaroni, A. A. Brown, and W. T. S. Huck, "Tunable wettability by clicking counterions into polyelectrolyte brushes," Adv. Mater. **19**, 151–154 (2007).

[29] O. Manor, I. U. Vakarelski, X. Tang, S. J. O'Shea, G. W. Stevens, F. Grieser, R. R. Dagastine, and D. Y. C. Chan, "Hydrodynamic boundary conditions and dynamic forces between bubbles and surfaces," Phys. Rev. Lett. **101**, 024501 (2008).

[30] O. Azzaroni, A. A. Brown, and W. T. S. Huck, "UCST wetting transitions of polyzwitterionic brushes driven by self-association," Angew. Chem. Int. Ed. **45**, 1770–1774 (2006).

[31] Y. J. Oh, E. S. Khan, A. Campo, P. Hinterdorfer, and B. Li, "Nanoscale Characteristics and Antimicrobial Properties of (SI-ATRP)-Seeded Polymer Brush Surfaces," ACS Appl. Mater. Interfaces **11**, 29312–29319 (2019).

[32] Droumaguet B. Gérard David Daskalaki, E. and K. Velonia, "Multifunctional giant amphiphiles via simultaneous copper(i)-catalyzed azide–alkyne cycloaddition and living radical polymerization," Chem. Comm. **48**, 1586–1588 (2012).

Origin of underwater oil-repellence in polyelectrolyte brush surfaces

Dan Daniel,* Shermin Simin Goh, Truong Ngoc Bao Tran, Xue Qi Koh, and Nikodem Tomczak†

Institute of Materials Research and Engineering,

*A*STAR (Agency for Science, Technology and Research),*

2 Fusionopolis Way, Innovis, Singapore 138634

* daniel@imre.a-star.edu.sg

† tomczakn@imre.a-star.edu.sg

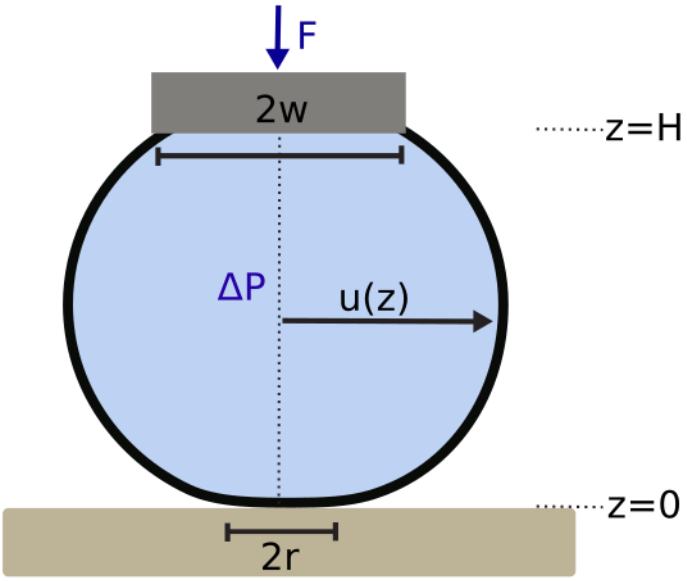

FIG. S1. Schematic of a droplet being compressed.

To model the droplet deformation of volume V due to the applied force F, we can solve the Young-Laplace equation

$$\frac{u''}{(1+u'^2)^{3/2}} - \frac{1}{u\sqrt{1+u'^2}} = -\Delta P/\gamma \text{ for } z \in (0, H) \tag{S1}$$

subject to the boundary conditions

$$\begin{aligned} u(0) &= r \\ u(H) &= w \\ \int_0^H \pi u^2 dz &= V \\ F &= \pi r^2 \Delta P \end{aligned} \tag{S2}$$

where w is the width of the contact size on the AFM cantilever, r is the droplet's base radius, γ is the interfacial tension, and $\Delta \mathrm{P} \approx 2\gamma/R$ is the Laplace pressure (Supplementary Fig. S1).

There are several ways to solve this boundary value problem numerically. Here, we first

non-dimensionalize the problem with respect to the droplet's size R and interfacial tension γ

$$\begin{aligned} \hat{F} &= F\gamma^{-1}R^{-1} \\ \hat{u} &= uR^{-1} \\ \hat{r} &= rR^{-1} \\ \hat{V} &= VR^{-3} \\ \Delta\hat{P} &= \Delta P R\gamma^{-1}, \text{etc} \end{aligned} \tag{S3}$$

and hence, we get the non-dimensionalized Young-Laplace equation

$$\frac{\hat{u}''}{(1+\hat{u}'^2)^{3/2}} - \frac{1}{\hat{u}\sqrt{1+\hat{u}'^2}} = -\Delta\hat{P}; \text{for } \hat{z} \in (0, \hat{H}) \tag{S4}$$

subject to the boundary conditions

$$\begin{aligned} \hat{u}(0) &= \hat{r} \\ \hat{u}(\hat{H}) &= \hat{a} \\ \int_0^{\hat{H}} \pi\hat{u}^2 d\hat{z} &= \hat{V} \\ \hat{F} &= \pi\hat{r}^2\Delta\hat{P}. \end{aligned} \tag{S5}$$

Using the shooting method [1], we chose to frame the Young-Laplace equation as an initial value problem, with initial values

$$\begin{aligned} \hat{u}(0) &= \hat{r} \\ \hat{u}'(0) &= 0, \end{aligned} \tag{S6}$$

while requiring that

$$\hat{\mathbf{m}}(\hat{r}, \Delta\hat{P}, \hat{\gamma}) = \begin{pmatrix} \hat{u}(\hat{H}) - \hat{w} \\ \int_0^{\hat{H}} \pi\hat{u}^2 d\hat{z} - \hat{V} \end{pmatrix} = 0. \tag{S7}$$

This converts the boundary value problem into a root-finding problem of $\hat{\mathbf{m}} = 0$, which we can solve by numerically integrating equation S4 with Runge-Kutta method subject to the initial conditions in equation S6.

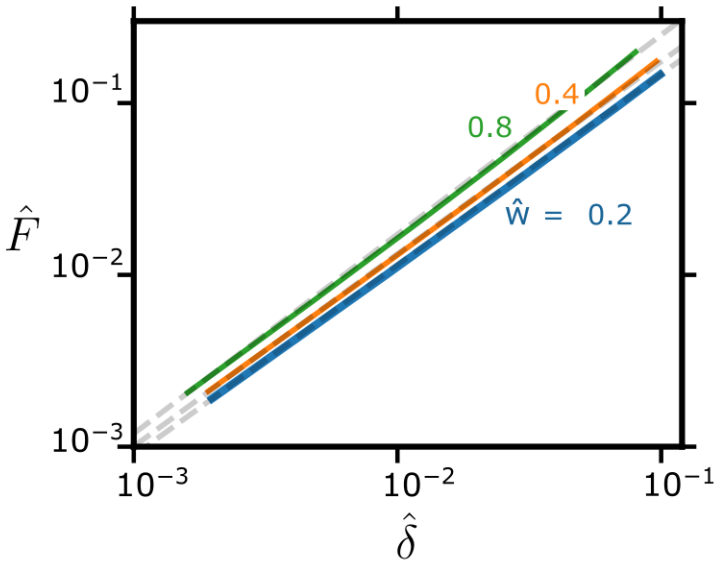

FIG. S2. Simulation results for non-dimensional $\hat{F}$ vs. $\hat{\delta}$ for different $\hat{w} = 0.2$, 0.4 and 0.8.

The simulation results are summarized in Figure S2 for different initial conditions, more specifically for different contact sizes $\hat{w} = 0.2$, 0.4 and 0.8. The numerical results can be fitted with power laws

$$\hat{F} = 1.9\,\hat{\delta}^{\,1.1}, 2.3\,\hat{\delta}^{\,1.12}, 3.6\,\hat{\delta}^{\,1.16} \tag{S8}$$

for $\hat{w} = 0.2$, 0.4 and 0.8, respectively (dashed lines in Figure S2). In the main text, for the results reported in Figure 3, $\hat{w} = 0.2$ and hence, we expect $F = 1.9\gamma R^{-0.1}\delta^{1.1}$ as reported in the main text.

The numerical calculations are implemented in Python code. See github repository for the codes used [2].

[1] J. Kiusalaas, *Numerical methods in engineering with Python 3* (Cambridge university press, 2013).

[2] D. Daniel, "Simulating droplet compression," `https://github.com/ddaniel331/simulating_compression` (2020), accessed: 2020-07-01.